

Article

Influences of the Decomposition Atmosphere and Heating Rate on the Pyrolysis Behaviors of Resin Sand

Qingwei Xu ^{1,*} , Yaping Zhu ¹, Kaili Xu ², Bingjun Li ¹  and Nan Su ^{1,*}¹ College of Information and Management Science, Henan Agricultural University, Zhengzhou 450046, China² School of Resources and Civil Engineering, Northeastern University, Shenyang 110819, China

* Correspondence: xuqingwei@henau.edu.cn (Q.X.); sunan@henau.edu.cn (N.S.)

Abstract: The pouring of sand casting is accompanied by severe heat conduction, and there is an urgent need to investigate the pyrolysis properties of foundry sand. The main purpose of this study was to investigate the pyrolysis behaviors of resin sand, including pre-coated sand (PCS), hot box sand (HBS), and warm box sand (WBS), at heating rates of 20 °C/min, 30 °C/min, and 40 °C/min in nitrogen and air atmospheres. The mass loss of the resin sand was monitored continuously with a simultaneous thermal analyzer, and the kinetic parameters of the resin sand were calculated based on the Coats–Redfern method and thermal data. The average mass loss of the resin sand during pyrolysis was 3.03%, which was much smaller than that of the other sands. The volatile release characteristic index of resin sand could not be calculated based on this concept. To solve this issue, the term T_{sto}/m_{loss} was established, and its value was determined. With increasing heating rates from 20 °C/min to 30 °C/min and from 30 °C/min to 40 °C/min, the mass losses of the resin sand increased by 0.79% and 0.64%, respectively, and the volatile release characteristic indices of the resin sand increased by 3.8×10^{-10} and 1.06×10^{-9} , respectively. In addition, the mass losses and volatile release characteristic indices of resin sand in an air atmosphere were greater than those in a nitrogen atmosphere. With increasing heating rate, the activation energy of the resin sand decreased in a nitrogen atmosphere. The findings concerning the thermal decomposition behaviors of resin sand provided a theoretical basis for the pouring step of the sand casting process.

Keywords: decomposition atmosphere; heating rate; resin sand; volatile release characteristic index; activation energy



Citation: Xu, Q.; Zhu, Y.; Xu, K.; Li, B.; Su, N. Influences of the Decomposition Atmosphere and Heating Rate on the Pyrolysis Behaviors of Resin Sand. *Buildings* **2024**, *14*, 1234. <https://doi.org/10.3390/buildings14051234>

Academic Editor: Boumediene Nedjar

Received: 21 March 2024

Revised: 24 April 2024

Accepted: 25 April 2024

Published: 26 April 2024



Copyright: © 2024 by the authors. Licensee MDPI, Basel, Switzerland. This article is an open access article distributed under the terms and conditions of the Creative Commons Attribution (CC BY) license (<https://creativecommons.org/licenses/by/4.0/>).

1. Introduction

Foundry manufacturing is a hot metal working process in which high-temperature molten metal is poured into a cavity to prepare castings [1,2]. In modern society, the foundry industry is the basis of modern machinery manufacturing and occupies an important position in the national economy and in social development. Sand casting, which occupies approximately 90% of the foundry industry, is the main method used for casting [3,4]. The main raw material consumed in sand casting is sand [4]. The highest demand for sand is in the construction industry, where it is used as concrete [5–7]. The physical properties of concrete have been studied comprehensively [8,9]. Sand casting promotes social and economic development but is accompanied by environmental pollution [10] and casualties [11]. Exploring the characteristics of foundry sand under high-temperature conditions is highly important for ensuring the safe production and quality of castings in the casting industry.

When high-temperature molten metal is poured into a cavity, the molten metal and the casting model undergo heat conduction [12–14], which causes the temperature of the casting model to increase rapidly. Moreover, certain materials, such as adhesives, curing agents, and coatings, in the sand are rapidly vaporized and pyrolyzed to produce gas. Heat conduction is a type of heat transfer that occurs within a substance or between objects with

different temperatures in direct contact without relative displacement [15–17] and involves the thermal movement of microscopic particles within a substance. The faster the increase in the temperature of the casting mold, the faster the vaporization and pyrolysis of these materials in the sand. Obtaining the variation in the temperature of the casting mold during pouring can help to gain a comprehensive understanding of the gas production of the casting mold under high-temperature conditions.

The methods for studying the variation in the temperature of casting molds can be categorized into experimental [11] and simulated methods [18]. With the development of computer technology, an increasing number of scholars have utilized computer software to simulate the complex features of the casting process [19,20]. Numerical simulation combines theoretical research with practical application and can simulate the temperature field, flow field, stress field, and microstructure, among other characteristics. The simulation results at a specific position at any moment can be displayed in the postprocessing stage. The algorithms for numerical simulation of casting mainly include the finite difference method (FDM) [21–23], the finite element method (FEM) [24–26], and the finite volume method (FVM) [27–29]. Different numerical algorithms have distinct discretization methods, boundary processing methods, and computational efficiencies and accuracies. The FDM is widely used in temperature field calculations of the casting solidification process and numerical simulations of the mold filling process. The FEM is mainly used for stress analysis in the casting process and for temperature and flow field analyses. Although the software can simulate temperature variations during pouring, it cannot effectively simulate the pyrolysis properties of foundry sand.

During real-world production, resin sand at a gate is pyrolyzed in an air atmosphere, and that in a cavity is thermally decomposed in a nitrogen atmosphere. From the inner wall to the outer wall of a sand mold, the heating rate of the resin sand gradually decreases. When the condition of the resin sand changes, its pyrolysis behavior changes. Previously, the thermal decomposition behaviors of foundry sand for cast iron were investigated at heating rates of 30 °C/min and 40 °C/min in a nitrogen atmosphere [30]. In another study, the thermal decomposition characteristics of foundry sand for cast steel were further investigated at heating rates of 20 °C/min, 30 °C/min, and 40 °C/min under nitrogen and air atmospheres [4]. However, these two research groups investigated only the pyrolysis characteristics of self-hardening resin sands and did not address other types of resin sands.

The volatile release characteristic index can be used to represent the pyrolysis reaction in the sample [31–33]. The volatile release characteristics of various materials, such as coal [34–36], oil [37–39], and biomass [40–42], have been widely studied. This parameter requires a specific initial temperature for volatile emissions and a corresponding mass loss rate of at least 0.1 mg/min [43]. In addition, the mass of the sample used for pyrolysis experiments is usually 5 mg [44]. Therefore, the initial temperature needs a mass loss rate of 2%/min. For foundry sand, the content of SiO₂ is approximately 94.6% [4], and the mass loss rate does not reach 2%/min. To address this issue, a new method can be adopted to calculate the volatile release characteristic index of foundry sand.

Kinetic parameters can be adopted to represent the physical and chemical characteristics of the material during heating [45–47], and these parameters can be calculated from pyrolysis data. The methods for calculating the kinetic parameters mainly include the distributed activation energy model (DAEM) [48–50], the Flynn–Wall–Ozawa (FWO) method [51–53], and the Coats–Redfern method [54–56]. The kinetic parameters of self-hardening resin sand can be calculated based on the Coats–Redfern method [4]. Different methods have distinct applications to pyrolysis for materials with various properties, and the change in the activation energy of the material is inconsistent with the change in the conversion rate [57–59]. For foundry sand, the validity of the calculated results of the kinetic parameters must be verified.

In summary, there are three highlights in this study compared with previous studies. First, the pyrolysis behaviors of a wide range of resin sands at different heating rates under nitrogen and air atmospheres were studied. Second, the term T_{stc}/m_{loss} was established,

and its value was determined; thus, the volatile release characteristic index of resin sand was calculated, and its validity was tested. Third, the kinetic parameters of the resin sand were calculated, and its validity was tested by one-way analysis of variance (ANOVA) [60].

2. Materials and Methods

2.1. Resin Sand Proportioning

The raw foundry sand used in this experiment was quartz sand, which originated from Gongyi, Henan Province, China, with a 007 model, a melting point of 2250 °C, a Moh hardness of 7.5, a density of 2.66 g/cm³, and a hydrochloric acid solubility of 3.5. Herein, the quartz sand consisted of particles formed by the crushing and processing of quartz stone. Quartz stone was a hard, wear-resistant, and chemically stable nonmetallic silicate mineral. Precoated sand (PCS), hot box sand (HBS), and warm box sand (WBS), which are commonly used, were taken as experimental objects, and their formulations are shown in Table 1.

Table 1. Proportion of resin sand.

Resin Sand	Adhesive		Curing Agent	
	Type	Content	Type	Content
PCS	Phenolic resin	2.5% (percentage of raw sand)	Hexamethylene tetramine	15% (percentage of phenolic resin)
HBS	Furan resin	2% (percentage of raw sand)	Ammonium chloride	30% (percentage of furan resin)
WBS	Furan resin	3% (percentage of raw sand)	Copper chloride	30% (percentage of furan resin)

PCS, also known as shell (core) sand, was mixed according to standard JB/T 8583-2008 [61]. The curing agent hexamethylene tetramine reacted with the water in the resin sand, producing formaldehyde and ammonia during heating. The generated formaldehyde reacted with phenolic resin, transforming the resin from a linear structure to a macromolecule with a three-dimensional structure. Ammonia formed an alkaline atmosphere, which was beneficial for this reaction.

HBS was mixed according to the standard JB/T 3823-2013 [62]. The curing agent ammonium chloride was weakly acidic after dissociation in water, and the acidity increased when heated. In addition, ammonium chloride reacted with free formaldehyde in furan resin to form hydrochloric acid, which accelerated the hardening of resin sand.

For WBS, the curing agent copper chloride aqueous solution was very stable at room temperature, began to decompose from 80 °C to 120 °C, and completely decomposed above 150 °C. The hardened resin sand had high strength, there was no need for secondary drying, and its hygroscopic properties were significantly improved.

2.2. Pyrolysis Experiments

An STA8000 Frontier instrument (PerkinElmer, WLM, USA) was used as a synchronous thermal analyzer for the pyrolysis of the resin sand. The mass loss of resin sand could be represented by the thermogravimetric (TG) curve, and the mass loss rate of resin sand could be represented by the differential thermogravimetric curve (DTG). DTG is the first derivative of the thermogravimetric curve.

The decomposition atmosphere of the resin sand pyrolysis experiment consisted of nitrogen and air (oxygen:nitrogen = 1:4); the heating rates were 20 °C/min, 30 °C/min, and 40 °C/min; and the temperature range was 25–1200 °C.

2.3. Volatile Release Characteristic Index

The volatile release characteristic index was used to represent the pyrolysis characteristics of the resin sand, and the calculation formula was as follows [16–18]:

$$D = \frac{(dw/dt)_{\max}(dw/dt)_{\text{mean}}}{T_s T_{\max} \Delta_{1/2}} \quad (1)$$

where D is the volatile release characteristic index; T_s is the initial temperature of volatile release, corresponding to the temperature at which the mass loss rate reached 0.1 mg/min, °C [19]; T_{max} is the temperature corresponding to the maximum mass loss rate of volatiles, °C; $(dw/dt)_{mean}$ is the average mass loss rate of volatiles, %/min; $(dw/dt)_{max}$ is the maximum mass loss rate of volatiles, %/min; and $\Delta_{1/2}$ is the temperature interval within the scope of $(dw/dt)/(dw/dt)_{max} = 1/2$, °C.

2.4. Kinetic Theory

The Coats–Redfern method is usually used to describe the thermal decomposition of materials [28–30]. According to the Arrhenius equation and the law of conservation of mass of materials, the kinetics theory of the reaction could be described as follows.

$$-\ln\left[\frac{-\ln(1-\alpha)}{T^2}\right] = \frac{E}{RT} - \ln\left(\frac{AR}{\beta E}\right) \quad (2)$$

where A is the preexponential factor, min^{-1} ; E is the activation energy, kJ/mol; R is the universal gas constant, 8.314 kJ/mol/K; T is the thermodynamic temperature, K; β is the heating rate, K/min; and α is the mass conversion rate of the pyrolysis reaction.

$$\alpha = \frac{m_0 - m_t}{m_0 - m_\infty} \quad (3)$$

where m_0 , m_∞ , and m_t are the initial mass of the sample, the final mass of the sample, and the mass of the sample at a specific time t , respectively.

For a given heating rate, the term $-\ln[-\ln(1-\alpha)/T^2]$ linearly varied as $1/T$ with a slope of E/R , and the intercept was $-\ln(AR/\beta E)$. The activation energy E was calculated with Equation (2).

3. Results

While heating resin sand, the adhesive, curing agent, and other materials are pyrolyzed and vaporized, which reduces the resin sand mass. The volatile release characteristic index is adopted to represent the pyrolysis behavior of the resin sand. A larger value indicates better resin sand release characteristics and an easier pyrolysis reaction in the sample [30]. The thermal decomposition experiment investigates the physical and chemical properties of the resin sand, and thermodynamic and kinetic principles are applied during research. The thermal decomposition kinetic parameters include the activation energy and preexponential factor [4]. The activation energy refers to the energy needed for molecules to move from a normal state to an active state prone to chemical reactions. In addition, the activation energy effectively reflects the material stability. The preexponential factor is determined by the thermal decomposition experiment, regardless of the reaction temperature or the substance concentration. To effectively understand the thermal decomposition results of the resin sand, the basic properties of the raw sand were tested first, including proximate, chemical composition, and particle diameter analyses.

3.1. Basic Properties of Raw Sand

3.1.1. Proximate Analysis

The proximate analysis of the raw sand is carried out according to the standard GB/T 30732-2014 [63]. The composition of the raw sand mainly includes ash (99.01%), volatiles (0.87%), and moisture (0.12%). However, fixed carbon is not detected.

3.1.2. Chemical Composition Analysis

To further test the raw sand, X-ray fluorescence (XRF) analysis is performed with a ZSX Primus II instrument (Rigaku, Japan), and the results are shown in Table 2.

Table 2. Chemical composition of the raw sand.

Chemical Composition	Content (%)	Chemical Composition	Content (%)	Chemical Composition	Content (%)
SiO ₂	96.174	SO ₃	0.196	CuO	0.018
Al ₂ O ₃	2.739	Fe ₂ O ₃	0.127	Cr ₂ O ₃	0.014
K ₂ O	0.654	Ag ₂ O	0.052	SrO	0.011

The results of the XRF analysis show that there are nine components of the raw sand, among which the SiO₂ content is the highest at 96.174%. Thus, SiO₂ is the main component of ash in the proximate analysis.

3.1.3. Particle Diameter Analysis

The influence of the particle diameter on the permeability of the molding sand is the most direct. The finer the particle diameter of the raw sand is, the lower the permeability of the molding sand. Therefore, the particle diameter of the raw sand significantly impacts the discharge of gas generated in the cavity during molten metal pouring. A laser particle size analyzer (model 3000; Malvern, UK) is used to determine the particle diameter of the raw sand according to the standard GB/T 15445.2-2006 [64], and the results are shown in Table 3.

Table 3. Results of the raw sand particle diameter.

Specific Surface Area	D [3,2]	D [4,3]	Dv (10)	Dv (50)	Dv (90)
24.30 m ² /kg	247 μm	291 μm	171 μm	278 μm	436 μm

D [3,2] indicates the average particle size of the surface area; D [4,3] indicates the average volumetric particle size; Dv (10) indicates that 10% of the particle size in the sample is less than this value; v indicates that the particle size is derived based on the volume distribution; Dv (50) indicates that 50% of the particle size in the sample is less than this value; and Dv (90) indicates that 90% of the particle size in the sample is less than this value.

The particle size distribution of the raw sand is shown in Figure 1.

The minimum and maximum particle sizes of the raw sand are 24.1 μm and 516 μm, respectively. The particle size of the raw sand increases from 24.1 μm to 272 μm as the bulk density gradually increases. When the particle size of the raw sand is 272 μm, its bulk density is the highest (13.55%), and the bulk density curve is roughly symmetric. The particle size of the raw sand increases from 272 μm to 516 μm as the bulk density gradually decreases.

The minimum particle size of the raw sand is 24.1 μm, which is greater than 20 μm, indicating that the raw sand does not contain mud.

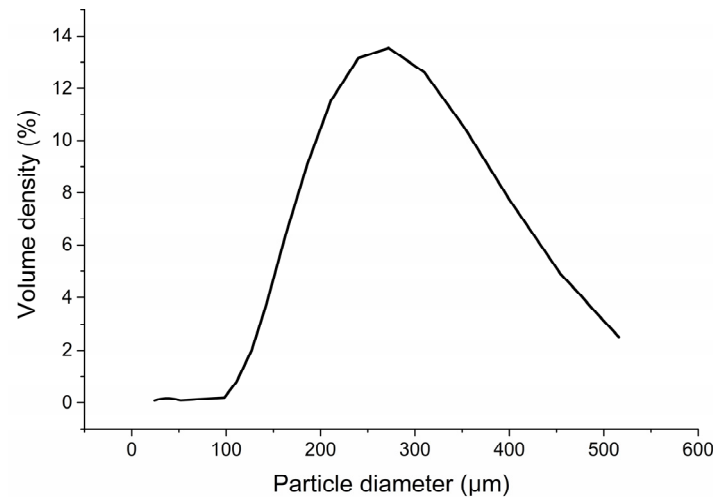


Figure 1. Particle size distribution of the raw sand.

3.2. Pyrolysis Behavior of Resin Sand

The thermal decomposition process of the resin sand is preliminarily analyzed, the decomposition atmosphere is set to nitrogen, the heating rate is 30 °C/min, and the temperature range is 25 °C–1200 °C. The pyrolysis process is shown in Figure 2. The thermal decomposition data of resin sand can be found in Supplementary Materials.

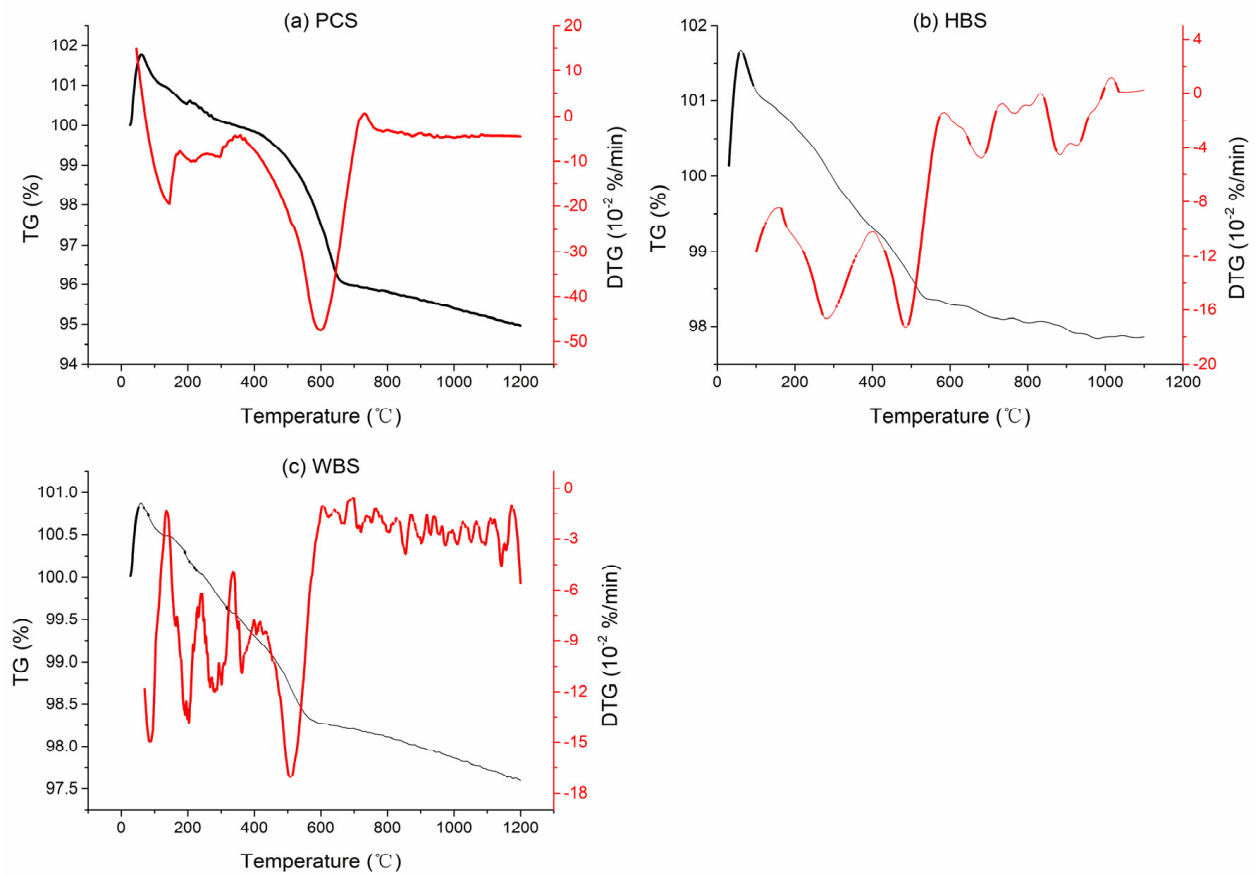


Figure 2. Thermal decomposition curves of the resin sand.

Figure 2 shows that there are significant differences in the pyrolysis processes of the three resin sands. The differences are mainly related to the pyrolysis characteristics of each resin sand, resulting in each resin sand exhibiting different pyrolysis behaviors. The

pyrolysis process of resin sand can be divided into three stages. In the first stage, the PCS ranges from 25 °C to 400 °C, the HBS and WBS range from 25 °C to 200 °C, and the dehydration reaction and volatilization of small molecular organic matter mainly occur during this stage. Notably, at this stage, due to the influences of buoyancy and convection, baseline drift occurs in the TG curve.

For the PCS in the first stage, depolymerization of phenolic resins produces phenol and its methyl substituents. In addition, the crosslinking of hydroxyl and methylene functional groups produces moisture and a small amount of CO.

In the second stage, the PCS ranges from 400 °C to 700 °C, and the HBS and WBS range from 200 °C to 600 °C. In this stage, the three different resin sands show obvious mass losses, and the adhesive and curing agent in the resin sand undergo drastic pyrolysis while releasing volatiles. The maximum mass loss rate of the PCS is the largest at $57.08 \times 10^{-2}\%/min$. The maximum mass loss rates of HBS and WBS are approximately the same at $19.25 \times 10^{-2}\%/min$ and $21.65 \times 10^{-2}\%/min$, respectively.

For PCS in the second stage, both crosslinking bond breaking and benzene ring rearrangement generate H₂, CH₄, CO, and H₂O. The benzene ring in the phenolic resin gradually condenses with increasing carbonization treatment temperature to form a thick polyphenylene ring structure with a high degree of polymerization.

Furan resin undergoes complex pyrolysis and polycondensation reactions, releasing small molecular gases, such as H₂O and CO. From 150 °C to 370 °C, polycondensation is generally accompanied by the combination and rearrangement of carbon atoms. From 370 °C to 570 °C, the intense pyrolysis of furan resin and the polycondensation reaction begin to slow. From 570 °C to 740 °C, the pyrolysis and polycondensation reactions of furan resin enter the final stage. The benzene ring in furan resin gradually polycondensates with increasing carbonization temperature, forming a polybenzene thick-ring structure with a high degree of polymerization [65].

In the third stage, the PCS ranges from 700 °C to 1200 °C, and the HBS and WBS range from 600 °C to 1200 °C. At this stage, the remaining adhesive, curing agent, and other materials in the resin sand continue to decompose slowly, and the quality of the resin sand is basically unchanged. The total mass losses of PCS, HBS, and WBS are 5.45%, 2.46%, and 2.63%, respectively.

For the PCS in the third stage, the unstable aromatic carbon is converted to a relatively stable carbon structure by a condensation reaction, releasing H₂ and small amounts of CO and moisture.

Above 740 °C, the molecular rearrangement and adjustment of the furan resin after coking occur. The polybenzene thick ring formed after the coking of furan resin experiences a microscopic transition state during the transformation to a graphite microcrystalline structure during carbonization. The furan resin precipitates graphite microcrystals at approximately 650 °C [65].

Table 1 shows that the contents of adhesive and curing agents in the WBS are the highest. The total mass loss during pyrolysis should be the largest, which seems to be inconsistent with the experimental results of this study. This result arises mainly due to the different mixing processes of the resin sand.

The sand mixing process for PCS requires the raw sand to be initially heated to 130–160 °C [66]. Then, phenolic resin is added to mix with the raw sand, and the resin melts and wraps around the surface of the sand grains. When the temperature of the sand decreases to 105–110 °C, the curing agent hexamethylene tetramine is added, and the mixture gradually cools.

The sand mixing process for HBS starts with mixing the raw sand with an aqueous solution of the curing agent ammonium chloride. Then, furan resin is added and mixed. Finally, the mixed sand is placed in the metal core box at a temperature of 200–250 °C [66]. When the core sand is heated, the adhesive furan resin on the surface of the sand grains hardens in a very short period by a condensation reaction.

The sand mixing process for WBS is similar to that for HBS; the raw sand is mixed with an aqueous solution of the curing agent copper chloride, furan resin is added and mixed, and the mixed sand is finally placed into the metal core box at a temperature of 150–220 °C [66]. The process of WBS can use the original HBS shooting machine, without additional equipment investment. Conversely, the original production process can be changed.

Greater mass loss from HBS and WBS occurs while mixing sand. Therefore, the final mass losses of HBS and WBS in this pyrolysis experiment are not as large as that of PCS.

3.3. Thermal Decomposition of Resin Sand in Nitrogen and Air Atmospheres

The thermal decomposition behaviors of the resin sand at a heating rate of 30 °C/min in nitrogen and air atmospheres are shown in Figure 3.

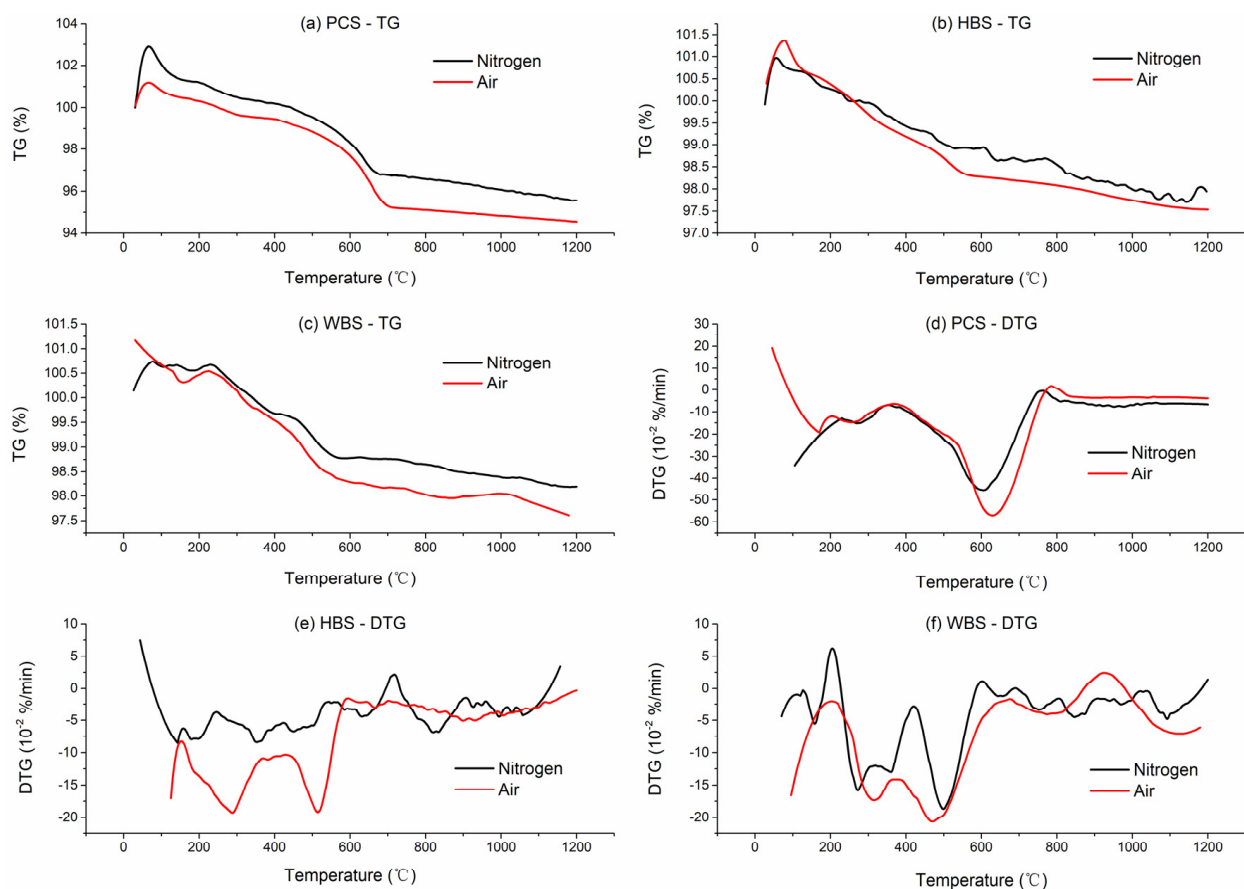


Figure 3. Pyrolysis of resin sand in nitrogen and air atmospheres.

Figure 3a–c show that the TG curve of resin sand pyrolysis continues to decrease with increasing temperature. In addition, the TG curve in an air atmosphere decreases more than that in a nitrogen atmosphere. The mass losses of PCS, HBS, and WBS in a nitrogen atmosphere are 4.45%, 2.06, and 1.81%, respectively, while those in an air atmosphere are 5.45%, 2.46%, and 2.39%, respectively.

Figure 3d–f show that there is a peak in the mass loss of the PCS at approximately 600 °C. The main reason is that the adhesive in the coated sand is pyrolyzed. The phenol hydroxyl group and methylene group form an ether bond or a C–C crosslinking bond through a condensation reaction to release H₂O molecules. However, the methylene bridge bond and ether bond connect to the benzene ring broke to form CO, CH₄, phenol, and its derivatives. Moreover, the benzene ring substances gradually form graphitic carbon structures.

The first mass loss peaks of HBS and WBS appear at approximately 300 °C in the air atmosphere. The main reason is that in HBS and WBS, the methylene or methine bridge connecting the furan resin chain starts to break when the temperature exceeds 250 °C. Furan resin undergoes a significant ring-opening reaction between 300 °C and 350 °C. The second peak of mass loss appears at approximately 500 °C. In the ring-opening reaction of furan resin, the amount of benzene increases significantly if the temperature exceeds 400 °C. The intermediate products of furan resin form benzene between 460 °C and 650 °C. In addition to benzene, the pyrolysis products of HBS and WBS include CO, CH₄, H₂O, CO₂, and other small gas molecules.

3.4. Thermal Decomposition of Resin Sand at Different Heating Rates

The thermal decomposition behaviors of the resin sand at heating rates of 20 °C/min, 30 °C/min, and 40 °C/min in an air atmosphere are shown in Figure 4.

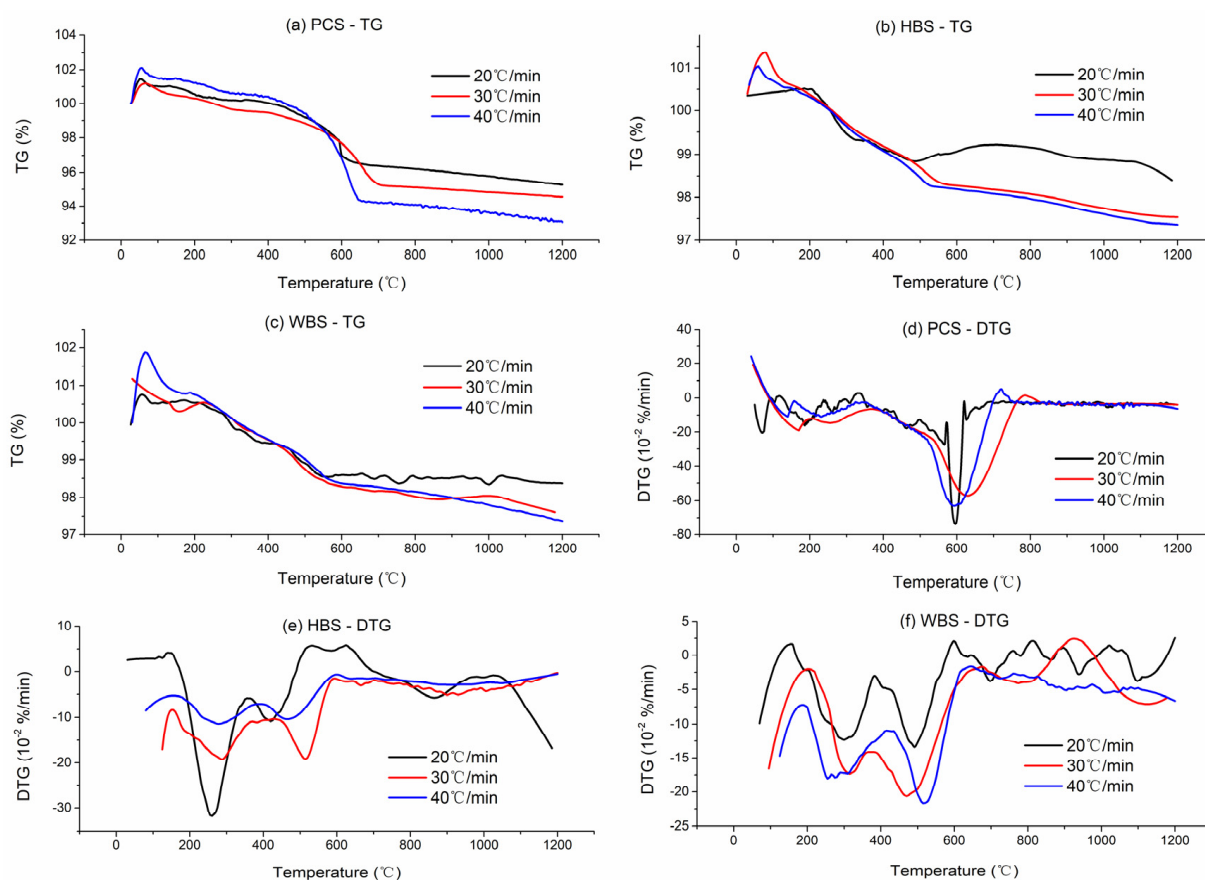


Figure 4. Thermal decomposition of the resin sand at heating rates of 20 °C/min, 30 °C/min, and 40 °C/min.

Figure 4a–c show that the TG curves of the resin sand continue to decrease with increasing temperature, and the higher the heating rate is, the greater the mass loss of the resin sand when the heating process ends. At heating rates of 20 °C/min, 30 °C/min, and 40 °C/min, the mass losses of PCS are 4.73%, 5.45%, and 6.95%; those of HBS are 1.6%, 2.46%, and 2.64%; and those of WBS are 1.63%, 2.39%, and 2.63%, respectively.

Figure 4d–f show that the mass loss rate of resin sand at different heating rates is relatively complicated. The mass loss peak of PCS is largest at a heating rate of 20 °C/min. The first mass loss peak of the HBS occurs at a heating rate of 20 °C/min. However, the second mass loss peak occurs at a heating rate of 30 °C/min. The two mass loss peaks of WBS basically increase with increasing heating rate. The main reason for this difference is

that different types of resin sand exhibit distinct pyrolysis behaviors under various heating rates, and the underlying reasons will be explored in future research.

3.5. Volatile Release Characteristic Index of Resin Sand

The volatile release characteristic index can be calculated based on the pyrolysis process of resin sand. Before calculating the volatile release characteristic index of resin sand, it is necessary to first determine the values of each parameter in Equation (1). The initial temperature T_s of volatile release refers to the temperature at which the mass loss rate of the sample during the pyrolysis experiment reaches 0.1 mg/min [19]. The initial mass of the sample is generally 5 mg for pyrolysis experiments [20], suggesting that the mass loss rate of the sample must reach 2%/min. After determining the rate of mass loss per minute, the initial temperature T_s is independent of the sample mass during the pyrolysis experiment. However, the maximum mass loss rate of the resin sand in this study is less than 2%/min. It is impossible to calculate the volatile release characteristic index of resin sand following this concept. The authors reported that T_{stv}/m_{loss} is 2.86%/min based on comprehensive research on the volatile release characteristic index of rice husks [15], where T_{stv} is the threshold for determining the initial temperature T_s ; specifically, this parameter is the percentage of mass loss of the sample per minute. m_{loss} is the mass loss of the sample during pyrolysis. The value of T_{stv} is 2%/min according to Equation (1). The threshold value of T_{stv} can be determined first based on the T_{stv}/m_{loss} ratio and the mass loss of the resin sand. The release characteristic index of the volatiles in the resin sand can be determined by combining Equation (1) with the remaining parameters, as shown in Table 4.

Table 4. Volatile release characteristics of the resin sand.

Resin Sand	Atmosphere	β (°C/min)	T_{stv} (%/min)	m_{loss} (%)	T_s (°C)	T_{max} (°C)	$(dw/d\tau)_{max}$ (%/min)	$(dw/d\tau)_{mean}$ (%/min)	$\Delta_{1/2}$ (°C)	D (% ² /min ² /°C ³)
PCS	Nitrogen	20	9.47×10^{-2}	3.31	453	607	34.18×10^{-2}	5.63×10^{-2}	241	2.90×10^{-10}
	Nitrogen	30	12.73×10^{-2}	4.45	430	605	45.58×10^{-2}	11.36×10^{-2}	280	7.11×10^{-10}
	Nitrogen	40	14.39×10^{-2}	5.03	459	597	47.56×10^{-2}	17.12×10^{-2}	224	1.33×10^{-9}
	Air	20	13.53×10^{-2}	4.73	452	596	73.76×10^{-2}	8.05×10^{-2}	233	9.46×10^{-10}
	Air	30	15.59×10^{-2}	5.45	465	630	57.08×10^{-2}	13.91×10^{-2}	265	1.02×10^{-9}
	Air	40	19.88×10^{-2}	6.95	492	591	63.06×10^{-2}	23.66×10^{-2}	181	2.83×10^{-9}
HBS	Nitrogen	20	4.46×10^{-2}	1.56	120	270	18.94×10^{-2}	2.66×10^{-2}	449	3.46×10^{-10}
	Nitrogen	30	5.89×10^{-2}	2.06	314	358	7.82×10^{-2}	5.26×10^{-2}	88	4.16×10^{-10}
	Nitrogen	40	6.12×10^{-2}	2.14	100	484	17.3×10^{-2}	7.28×10^{-2}	446	5.83×10^{-10}
	Air	20	4.58×10^{-2}	1.6	190	260	31.75×10^{-2}	2.72×10^{-2}	280	6.24×10^{-10}
	Air	30	7.04×10^{-2}	2.46	125	290	19.25×10^{-2}	6.28×10^{-2}	435	7.67×10^{-10}
	Air	40	7.55×10^{-2}	2.64	210	278	11.39×10^{-2}	8.99×10^{-2}	152	1.15×10^{-9}
WBS	Nitrogen	20	4.15×10^{-2}	1.45	236	501	11.72×10^{-2}	2.47×10^{-2}	303	8.08×10^{-11}
	Nitrogen	30	5.18×10^{-2}	1.81	440	499	18.68×10^{-2}	4.62×10^{-2}	122	3.22×10^{-10}
	Nitrogen	40	6.89×10^{-2}	2.41	344	509	17.12×10^{-2}	6.15×10^{-2}	219	3.66×10^{-10}
	Air	20	4.66×10^{-2}	1.63	405	491	13.4×10^{-2}	2.77×10^{-2}	141	1.32×10^{-10}
	Air	30	6.84×10^{-2}	2.39	255	470	20.65×10^{-2}	8.13×10^{-2}	325	3.23×10^{-10}
	Air	40	7.52×10^{-2}	2.63	200	515	21.65×10^{-2}	8.95×10^{-2}	385	4.89×10^{-10}

As shown in Table 4, the volatile release characteristic index D of the resin sand increases with increasing heating rate under both nitrogen and air atmospheres. In addition, the volatile release characteristic index of resin sand is greater in an air atmosphere than in a nitrogen atmosphere. This difference suggests that increasing the heating rate in the air atmosphere is favorable for the pyrolysis of resin sand.

3.6. Kinetics Analysis of Resin Sand

By taking the term $(1/T) \times 10^3$ as the independent variable and the term $-\ln[-\ln(1 - \alpha)/T^2]$ as the dependent variable, an equation can be fitted. The activation energy E and prefactor A of the resin sand can be calculated by calculating the slope and intercept of the linear equation, as shown in Table 5.

Table 5. Kinetics parameters of the resin sand.

Resin Sand	Atmosphere	β (°C/min)	Equation	E (KJ/mol)	A (min ⁻¹)	Pearson's R
PCS	Nitrogen	20	$y = 9.20973x + 3.34242$	76.57	6.4364	0.99951
	Nitrogen	30	$y = 8.56259x + 4.43528$	71.19	3.0097	0.99886
	Nitrogen	40	$y = 8.14836x + 4.55662$	67.75	3.3826	0.99627
	Air	20	$y = 6.90464x + 6.0716$	57.41	0.3151	0.99848
	Air	30	$y = 8.52829x + 4.34177$	70.9	3.2912	0.98984
	Air	40	$y = 11.96321x + 0.25952$	99.46	364.7619	0.99414
HBS	Nitrogen	20	$y = 6.46881x + 3.47767$	53.78	3.9489	0.9276
	Nitrogen	30	$y = 4.10173x + 8.0692$	34.10	0.0381	0.98829
	Nitrogen	40	$y = 3.73828x + 8.49313$	31.08	0.0303	0.99539
	Air	20	$y = 4.65897x + 5.71185$	38.73	0.3046	0.85406
	Air	30	$y = 7.11362x + 2.55222$	59.14	16.4324	0.94223
	Air	40	$y = 2.36259x + 10.39441$	19.64	0.0029	0.98806
WBS	Nitrogen	20	$y = 7.02694x + 4.53135$	58.42	1.4957	0.99852
	Nitrogen	30	$y = 6.04784x + 6.07901$	50.28	0.4109	0.98954
	Nitrogen	40	$y = 3.16716x + 9.52065$	26.33	0.0092	0.98868
	Air	20	$y = 4.79026x + 6.95508$	39.83	0.0904	0.95085
	Air	30	$y = 4.88472x + 7.31655$	40.61	0.0963	0.99825
	Air	40	$y = 3.86463x + 9.02241$	32.13	0.0184	0.99221

The fitting effect of the equation can be roughly determined by the Pearson correlation coefficient. In Table 5, except for one fitting equation with a correlation coefficient of 0.854, the correlation coefficients of the remaining equations all exceed 0.92, indicating that the fitting effect of the equations is good. To strictly test the fitting effect of the equation, it is necessary to conduct one-way ANOVA for the error source, as shown in Table 6.

By taking the results of one-way ANOVA of PCS in a nitrogen atmosphere at a heating rate of 20 °C/min as an example, $F_{0.05}(1164) = 3.84 < 16,7906$, indicating that the independent variable significantly influences the dependent variable. In addition, $p = 0 < 0.05$ indicates that the independent variable significantly impacts the dependent variable. Therefore, the independent variable of the fitting equation of the pyrolysis kinetics parameters of PCS significantly influences the dependent variable in the nitrogen atmosphere and at a heating rate of 20 °C/min, indicating that the linear fitting equation selected is accurate and effective. Similar tests can be carried out, and the fitting equations of the pyrolysis kinetic parameters of PCS, HBS, and WBS under other conditions are accurate and effective.

The activation energies of PCS, HBS, and WBS decrease with increasing heating rate in a nitrogen atmosphere, indicating that the energy required for the conversion of volatiles in resin sand to an active state is reduced. Moreover, increasing the heating rate is conducive to the pyrolysis of resin sand in a nitrogen atmosphere.

Overall, the activation energy of PCS is the largest in the nitrogen atmosphere, the activation energy of WBS is the second largest, and the activation energy of HBS is the smallest. This trend is mainly related to the sand mixing processes of the three types of resin sand. During sand mixing, the HBS must be heated to 200–250 °C, the WBS must be heated to 150–220 °C, and the PCS must be heated to 130–160 °C [66]. The higher the temperature of resin sand heating is, the more energy it receives, and the smaller the energy required to activate volatiles during pyrolysis; specifically, the activation energy is reduced.

The activation energy of resin sand does not regularly change with the heating rate in an air atmosphere. The activation energy of PCS increases with increasing heating rate, while the activation energies of HBS and WBS first increase and then decrease with increasing heating rate. These results indicate that the pyrolysis of resin sand in an air atmosphere is complicated, and future research must address this issue.

Table 6. Results of one-way ANOVA.

Resin Sand	Atmosphere	Heating Rate (°C/min)	Source of Variation	Degrees of Freedom	Sum of Squares	Mean Square	F	p		
PCS	Nitrogen	20	Model error	1	59.18393	59.18393	167,906.48309	0		
			Random error	164	0.05781	3.52×10^{-4}				
			Total	165	59.24174					
		30	Model error	1	6.62679	6.62679			1341.49912	0
			Random error	30	0.1482	0.00494				
			Total	31	6.77498					
		40	Model error	1	29.29323	29.29323			18,543.40404	0
			Random error	139	0.21958	0.00158				
			Total	140	29.51281					
	Air	20	Model error	1	11.31318	11.31318	34,399.36928	0		
			Random error	105	0.03453	3.29×10^{-4}				
			Total	106	11.34771					
		30	Model error	1	3.98285	3.98285	1163.29093	0		
			Random error	24	0.08217	0.00342				
			Total	25	4.06502					
40	Model error	1	79.84294	79.84294	12,942.34202	0				
	Random error	153	0.94388	0.00617						
	Total	154	80.78682							
HBS	Nitrogen	20	Model error	1	35.34264	35.34264	684.38759	0		
			Random error	111	5.73218	0.05164				
			Total	112	41.07482					
		30	Model error	1	5.0071	5.0071	3524.06109	0		
			Random error	84	0.11935	0.00142				
			Total	85	5.12645					
		40	Model error	1	4.80542	4.80542	11,094.87771	0		
			Random error	103	0.04461	4.33×10^{-4}				
			Total	104	4.85003					
	Air	20	Model error	1	2.70073	2.70073	45.82843	3.27×10^{-6}		
			Random error	17	1.00183	0.05893				
			Total	18	3.70256					
		30	Model error	1	5.25536	5.25536	126.59337	5.20×10^{-9}		
			Random error	16	0.66422	0.04151				
			Total	17	5.91958					
40	Model error	1	3.82119	3.82119	5346.67629	0				
	Random error	130	0.09291	7.15×10^{-4}						
	Total	131	3.9141							
WBS	Nitrogen	20	Model error	1	35.31583	35.31583	45,584.93196	0		
			Random error	135	0.10459	7.75×10^{-4}				
			Total	136	35.42042					
		30	Model error	1	30.9454	30.9454	7056.08741	0		
			Random error	150	0.65784	0.00439				
			Total	151	31.60325					
		40	Model error	1	7.37748	7.37748	6121.59332	0		
			Random error	141	0.16993	0.00121				
			Total	142	7.5474					
	Air	20	Model error	1	35.82054	35.82054	1659.41313	0		
			Random error	176	3.79918	0.02159				
			Total	177	39.61973					
		30	Model error	1	7.95686	7.95686	9420.3247	0		
			Random error	33	0.02787	8.45×10^{-4}				
			Total	34	7.98473					
40	Model error	1	3.26363	3.26363	1967.6818	0				
	Random error	31	0.05142	0.00166						
	Total	32	3.31505							

4. Discussion

3.7. Comparison with Previous Studies

The main component of foundry sand is ash, the contents of volatiles and moisture are very low, and fixed carbon is not detected [4,30]. These results are consistent with those of this study. Murthy and Rao tested the chemical components of quartz sand and found that the content of SiO₂ accounts for 96.62% of the total content [67], which is basically consistent with our results. For foundry sand dust, the content of SiO₂ is approximately

50% [68]. Additional impurities are mixed in the foundry sand dust during the shakeout process, which sharply decreases the SiO₂ content. Only the proximate analysis of the raw sand was carried out in Ref. [30], and proximate and chemical composition analyses of the raw sand were carried out in Ref. [4]. In addition to the proximate and chemical composition analyses of the raw sand, a particle diameter analysis of the raw sand was carried out. The results showed that the raw sand does not contain mud, indicating that the raw sand is of high quality.

The mass loss of biomass can reach approximately 75% during thermal decomposition [69–71]. The main component of resin sand is silica, which is stable in high-temperature environments; thus, the total mass loss of resin sand is much smaller than that of biomass. During the pyrolysis of self-hardening resin sand, the maximum mass loss is 2.24% [30], which is basically consistent with the results of this study, indicating that the mass loss during the pyrolysis of resin sand is very small with high-temperature stability.

The mass loss of the resin sand in the air atmosphere is greater than that in the nitrogen atmosphere because the adhesive and curing agent in the resin sand is prone to pyrolysis in the air atmosphere. The mass loss of self-hardening resin sand in an air atmosphere is greater than that in a nitrogen atmosphere [30], which is consistent with the results of this paper.

Although the mass loss of resin sand increases with increasing heating rate, the total mass loss of resin sand during heating is still lower than that of other materials [71–73]. The main component of resin sand, silicon dioxide, has high-temperature stability, and its mass loss is not large in a high-temperature environment. This phenomenon is conducive to the casting process. During the thermal decomposition experiment, with increasing heating rate, the residual mass of the resin decreases [74]. Therefore, increasing the heating rate is conducive to the thermal decomposition of the material, which is consistent with the results of this paper. Reportedly, by pyrolyzing self-hardening resin sand, increasing the heating rate is prone to the pyrolysis of foundry sand [4,30]. In this study, pyrolysis experiments of different types of resin sand at different heating rates were carried out, and the conclusions are valuable.

The volatile release characteristic index of self-hardening resin sand in a nitrogen atmosphere increases with increasing heating rate, and it is greater in an air atmosphere than in a nitrogen atmosphere at a heating rate of 20 °C/min [4], which is consistent with the results of this study. This study involves a comprehensive investigation of the volatile release characteristics of resin sand through pyrolysis experiments under different heating rates and decomposition atmosphere conditions with different types of resin sand. The results are convincing. Compared with other materials, the volatile release characteristic index of resin sand is very small, approximately one millionth to one-tenth that of other materials [31–33]. Compared with other materials, resin sand is difficult to pyrolyze under high-temperature conditions. The volatile content of resin sand is very low, and the main component SiO₂ has high-temperature stability, which is conducive to maintaining the stability of molding sand during casting. These results are consistent with the analyses of the TG and DTG curves of the resin sand.

The activation energy of PCS in a nitrogen atmosphere at a heating rate of 20 °C/min is roughly equal to that of corncob [44] but much less than that of solid waste and lignite [75]. The average mass loss of resin sand during pyrolysis is 3.03%, while the mass loss of biomass during pyrolysis is approximately 75% [44]. In addition, the mass loss of solid waste can reach 90% [75]. The main component of the resin sand in this study is silica, which has high-temperature stability. Furthermore, the volatile content is very low, and the number of volatiles that can be converted into an active state is relatively low. Therefore, the activation energy required in the main pyrolysis stage is low. In the pyrolysis stage of other materials (biomass, solid waste, etc.), most of the mass is converted into volatile dispersion loss in an active state; thus, the activation energy requirements are relatively great. With increasing heating rate, the activation energy of self-hardening resin sand in a nitrogen atmosphere gradually decreases [4], which is consistent with the results of this study. In

this study, the activation energy of resin sand was investigated in pyrolysis experiments of different types of resin sand at different heating rates, and the results are valuable.

The activation energy of self-hardening resin sand in an air atmosphere is greater than that in a nitrogen atmosphere [4]. However, this conclusion is obtained at only one heating rate, providing weak evidence. Overall, there is no regular causal relationship between the activation energy and the heating rate of resin sand in an air atmosphere. Some scholars have reported that the activation energy of materials in an air atmosphere is greater than that in a nitrogen atmosphere [76], but other scholars have found opposing support [77]. To investigate the changes in the activation energy of materials, some scholars have conducted thermal decomposition experiments on materials with different oxygen contents [78]. The results showed that the activation energy of materials changes unstably with increasing oxygen content. The activation energy of the material increases steadily with increasing mass conversion rate and decreases when the activation energy peaks [79].

3.8. Limitations

First, only the pyrolysis behaviors of resin sand in nitrogen and air atmospheres were investigated. Further attention should be given to the influences of oxygen content on the thermal decomposition characteristics of resin sand. Second, the activation energy of resin sand does not change regularly with the heating rate in an air atmosphere, and future studies should focus on this issue. Third, the mass loss of resin sand occurs during the sand mixing process, and future studies should consider this issue.

4. Conclusions

The main component of the resin sand is SiO_2 , which has high-temperature stability. Increasing the heating rate in an air atmosphere is conducive to the pyrolysis of resin sand. The average mass loss of the resin sand during pyrolysis is 3.03%, which is much smaller than that of the other materials. The term T_{stv}/m_{loss} is equivalent to 2.86%/min, and the volatile release characteristic index of resin sand can be calculated. The value of this parameter is even smaller than that of other materials. The validity of the kinetic parameters of the resin sand was tested by one-way ANOVA.

Supplementary Materials: The following supporting information can be downloaded at <https://www.mdpi.com/article/10.3390/buildings14051234/s1>: The thermal decomposition data have been uploaded as electronic Supplementary Material.

Author Contributions: Data collection, Methodology, Writing—review and editing: Q.X.; Methodology: Y.Z., Investigation: K.X., Formal analysis: B.L., Data curation, Review and editing: N.S. All authors have read and agreed to the published version of the manuscript.

Funding: This study was supported by the Natural Science Foundation of Henan (Grant No. 232300420297), General Program of Humanities and Social Sciences Research in Henan Universities (Grant No. 2024-ZDJH-035), Research Innovation Fund of Henan Agricultural University in Philosophy and Social Sciences (Grant No. SKJJ2022B06), Major Program of Philosophy and Social Science Basic Research in Higher Education Institutions in Henan Province (Grant No. 2024-JCZD-21), and Research and Practice Program on Research Teaching Reform in Undergraduate Colleges and Universities in Henan Province (Grant No. 2022SYJXLX017).

Data Availability Statement: The data presented in this study are available in Supplementary Materials.

Conflicts of Interest: The authors declare no conflicts of interest.

References

1. Tang, H.; Zhang, W.; Li, X.; Wei, S. A discrete group teaching optimization algorithm for solving many-objective sand casting whole process production scheduling problem. *Comput. Oper. Res.* **2024**, *164*, 106563. [[CrossRef](#)]
2. Yu, J.; Zhang, Y.; Guo, J.; Shu, X.; Lu, Q.; Chen, Q. Sand casting-inspired surface modification of 3D-printed porous polyetheretherketone scaffolds for enhancing osteogenesis. *Compos. Part A-Appl. Sci. Manuf.* **2024**, *179*, 108033. [[CrossRef](#)]

3. Xu, Q.; Xu, K.; Li, L.; Xu, X.; Yao, X. Energy release and countermeasures for sand casting explosion accidents. *Hum. Ecol. Risk Assess.* **2020**, *26*, 2078–2090. [[CrossRef](#)]
4. Chen, S.; Zhang, J.; Xu, K.; Xu, Q. Thermal Decomposition Behaviour of Foundry Sand for Cast Steel in Nitrogen and Air Atmospheres. *Math. Probl. Eng.* **2020**, *2020*, 8121276. [[CrossRef](#)]
5. Meskhi, B.; Beskopylny, A.N.; Stel'makh, S.A.; Shcherban, E.; Mailyan, L.R.; Shilov, A.A.; El'shaeva, D.; Shilova, K.; Karalar, M.; Aksoylu, C.; et al. Analytical Review of Geopolymer Concrete: Retrospective and Current Issues. *Materials* **2023**, *16*, 3792. [[CrossRef](#)]
6. Celik, A.I.; Tunc, U.; Bahrami, A.; Karalar, M.; Mydin, M.A.O.; Alomayri, T.; Ozkilog, Y.O. Use of waste glass powder toward more sustainable geopolymer concrete. *J. Mater. Res. Technol.-JMRT* **2023**, *24*, 8533–8546. [[CrossRef](#)]
7. Ozkilog, Y.O.; Celik, A.I.; Tunc, U.; Karalar, M.; Deifalla, A.; Alomayri, T.; Althoey, F. The use of crushed recycled glass for alkali activated fly ash based geopolymer concrete and prediction of its capacity. *J. Mater. Res. Technol.-JMRT* **2023**, *24*, 8267–8281. [[CrossRef](#)]
8. Madenci, E.; Fayed, S.; Mansour, W.; Ozkilog, Y.O. Buckling performance of pultruded glass fiber reinforced polymer profiles infilled with waste steel fiber reinforced concrete under axial compression. *Steel Compos. Struct.* **2022**, *45*, 653–663.
9. Fayed, S.; El-din, A.B.; Basha, A.; Mansour, W. Shear behavior of RC pile cap beams strengthened using ultra-high performance concrete reinforced with steel mesh fabric. *Case Stud. Constr. Mater.* **2022**, *17*, e01532. [[CrossRef](#)]
10. Chakraborty, P.; Wood, D.A.; Sinh, S.; Hzara, B. Trace element contamination in soils surrounding the open-cast coal mines of eastern Raniganj basin, India. *Environ. Geochem. Health* **2023**, *45*, 7275–7302. [[CrossRef](#)]
11. Xu, Q.; Xu, K. Safety assessment of sand casting explosion accidents through on-site testing and numerical simulation of the temperature variation in sand molds to protect employee health. *Process Saf. Environ. Prot.* **2022**, *159*, 452–463. [[CrossRef](#)]
12. Wang, X.; Zhang, T.; Zhang, R.; Wang, X.; Yuan, Y.; Li, Z.; Han, Z. Study on the heat transfer at the casting-mould interface in resin-bonded sand mould casting of Mg-Gd-Y-Zr alloy. *Int. J. Cast Met. Res.* **2020**, *33*, 1–10. [[CrossRef](#)]
13. Jeon, J.H.; Bae, D.H. Effect of cooling rate on the thermal and electrical conductivities of an A356 sand cast alloy. *J. Alloys Compd.* **2019**, *808*, 151756. [[CrossRef](#)]
14. Li, Y.; Hu, A.; Fu, Y.; Liu, S.; Shen, W.; Hu, H.; Nie, X. Al Alloys and Casting Processes for Induction Motor Applications in Battery-Powered Electric Vehicles: A Review. *Metals* **2022**, *12*, 216. [[CrossRef](#)]
15. Hua, Y.; Luo, L.; Le Corre, S.; Fan, Y. Machine-learning topology optimization with stochastic gradient descent optimizer for heat conduction problems. *Int. J. Heat Mass Transf.* **2024**, *223*, 125226. [[CrossRef](#)]
16. Weng, L.; Xu, F.; Chen, X. Three-dimensional analysis of thermoelastic damping in couple stress-based rectangular plates with nonlocal dual-phase-lag heat conduction. *Eur. J. Mech. A-Solids* **2024**, *105*, 105223. [[CrossRef](#)]
17. Bar-Kohany, T.; Jain, A. Dissipation of boundary effects in multilayer heat conduction problems. *Int. J. Heat Mass Transf.* **2024**, *223*, 125207. [[CrossRef](#)]
18. Ammar, A.; Ben Saada, M.; Cueto, E.; Chinesta, F. Casting hybrid twin: Physics-based reduced order models enriched with data-driven models enabling the highest accuracy in real-time. *Int. J. Mater. Form.* **2024**, *17*, 16. [[CrossRef](#)]
19. Wang, M.; Zheng, L.; Kang, H. 3-Dimensional conformal cooling channel design: Origami-inspired topology optimization approach. *Appl. Therm. Eng.* **2024**, *242*, 122526. [[CrossRef](#)]
20. Ringel, A.; Hirt, G. Bending behavior of structured steel sheets with undercuts for interlocking with Al die-cast metal. *Int. J. Mater. Form.* **2024**, *17*, 2. [[CrossRef](#)]
21. Zong, H.; Cong, Q.; Zhang, T.; Hao, Y.; Xiao, L.; Hao, G.; Zhang, G.; Guo, H.; Hu, Y.; Jiang, W. Simulation of printer nozzle for 3D printing TNT/HMX based melt-cast explosive. *Int. J. Adv. Manuf. Technol.* **2022**, *119*, 3105–3117. [[CrossRef](#)]
22. Yan, B.; Wang, R.; Ding, B.; Wang, Y. Numerical simulation analysis of tunnel backfill grout based on DEM-FDM coupling and particle inlet. *Undergr. Space* **2024**, *14*, 285–299. [[CrossRef](#)]
23. Yohannan, A.; Vincent, S.; Divakaran, N.; Venugopal, A.K.P.; Patra, S.; Ashish, K.; Mohanty, S. Experimental and simulation studies of hybrid MWCNT/montmorillonite reinforced FDM based PLA filaments with multifunctional properties enhancement. *Polym. Compos.* **2024**, *45*, 507–522. [[CrossRef](#)]
24. Narayanan, S.; Sahani, P.; Rathod, J.; Soma, V.R.; Yalla, R.; Tata, B.V.R. Thin photonic crystal templates for enhancing the SERS signal: A case study using very low concentrations of dye molecules. *Phys. Scr.* **2024**, *99*, 35512. [[CrossRef](#)]
25. Takemura, K.; Sudo, K.; Dorget, R.; Dadiel, J.L.; Sakafuji, M.; Yokoyama, K.; Oka, T.; Sakai, N. Study on the PFM Behavior of GdBCO Bulk Joined by ErBCO and Its FEM Simulation. *IEEE Trans. Appl. Supercond.* **2024**, *34*, 6800405. [[CrossRef](#)]
26. Szucs, H. Numerical study to investigate the thermal characteristic length with coupled CFD-FEM simulations. *Int. J. Heat Fluid Flow* **2024**, *106*, 109312. [[CrossRef](#)]
27. De Andrade, G.S.; Nascimento, E.J.G.; de Lemos, M.J.S. Transient heat transfer in concentric cylinders using periodic boundary condition and asymmetric heat generation applied to thermal plug and abandonment of oil wells. *Int. J. Therm. Sci.* **2024**, *196*, 108689. [[CrossRef](#)]
28. Xu, Y.; Yang, G.; Hu, D. Comparison of surface tension models for the simulation of two-phase flow in an ISPH-FVM coupling method. *Eur. J. Mech. B-Fluids* **2024**, *105*, 57–96. [[CrossRef](#)]
29. Liu, S.; Yang, G.; Xu, Y.; Hu, D. A SPH-FVM coupling method based on triangular mesh for the simulation of two-phase flows. *Eng. Anal. Bound. Elem.* **2024**, *159*, 237–258. [[CrossRef](#)]

30. Xu, Q.; Xu, K.; Yao, X.; Li, J.; Li, L. Thermal decomposition characteristics of foundry sand for cast iron in nitrogen atmosphere. *R. Soc. Open Sci.* **2018**, *5*, 181091. [[CrossRef](#)]
31. Yang, L.; Zhang, Z.; Chen, A.; Mao, W.; Zhu, Z.; Zhao, Y.; Zhang, L. Experimental and kinetic study on pyrolysis and combustion characteristics of pesticide waste liquid. *J. Environ. Chem. Eng.* **2024**, *12*, 111994. [[CrossRef](#)]
32. Zhang, X.; Liu, Q.; Kong, B.; Bultinck, T.; Lu, W. Characterizing emissions of VOCs from the initial degradation of kitchen waste in household waste bins of residential areas in Beijing. *J. Hazard. Mater.* **2024**, *466*, 133479. [[CrossRef](#)] [[PubMed](#)]
33. Sun, Y.; Du, C.; Chen, G.; Kumar, A.; Wu, S.; Cheng, Z.; Yan, B.; Chen, G.Y. Co-disposal kinetics and characteristics of sewage sludge and municipal solid waste incineration fly ash. *J. Anal. Appl. Pyrolysis* **2024**, *177*, 106319. [[CrossRef](#)]
34. Zhu, Z.; Huang, Y.; Yu, M.; Gao, J.; Cheng, H.; Li, Z.; Xu, W.; Xiao, Y. Co-combustion of bituminous coal and industrious sludge under non-isothermal and isothermal conditions: Thermal behaviors, kinetic analyses, and heavy metals migration. *J. Clean. Prod.* **2024**, *434*, 140167. [[CrossRef](#)]
35. Li, J.; Hu, X.; Qiao, X. Thermogravimetric experimental study on the co-combustion of coal gangue and polypropylene. *Thermochim. Acta* **2024**, *732*, 179660. [[CrossRef](#)]
36. Zhang, Y.; Yang, Y.; Wang, G.; Li, P.; Liu, H.; Wang, H.; Gao, K. Changes in physical and chemical structure and Full-stage oxidation characteristics of coal caused by igneous intrusion. *Energy* **2024**, *288*, 129780. [[CrossRef](#)]
37. Ogradowska, D.; Damerau, A.; Banaszczyk, P.; Tanska, M.; Konopka, I.Z.; Pilat, B.; Dajnowiec, F.; Linderborg, K.M. Native and pregelatinized potato and rice starches and maltodextrin as encapsulating agents for linseed oil ethyl esters-Comparison of emulsion and powder properties. *J. Food Eng.* **2024**, *364*, 111799. [[CrossRef](#)]
38. Cao, R.; Yang, D.; Kang, Z.; Huang, D.; Cui, Z.; Lu, Y. Effects of Inherent Minerals on Pyrolysis Behavior and Kinetics of Jimsar Oil Shale. *ACS Omega* **2023**, *8*, 40396–40406. [[CrossRef](#)]
39. Yang, Y.; Luo, Z.; Ding, X.; Zhang, F.; Luo, C.; Zhang, H.; Shu, C. Effects of dust concentration, particle size, and crude oil concentration on the explosion characteristics of oil-immersed coal dust. *Fuel* **2024**, *356*, 129596. [[CrossRef](#)]
40. Sun, Y.; Zhang, X.; Yu, Q.; Yang, T.; Yan, B.; Li, R.; Chen, G. Effect of pickling on pyrolysis characteristics and adsorption properties of biomass. *Energy Sources Part A-Recovery Util. Environ. Eff.* **2024**, *46*, 228–243. [[CrossRef](#)]
41. Liu, Q.; Sun, J.; Gu, Y.; Zhong, W.; Gao, K. Experimental study on CO₂ co-gasification characteristics of biomass and waste plastics: Insight into interaction and targeted regulation method. *Energy* **2024**, *292*, 130509. [[CrossRef](#)]
42. Yahya, A.M.; Adeleke, A.A.; Nzerem, P.; Ikubanni, P.P.; Ayuba, S.; Rasheed, H.A.; Gimba, A.; Okafor, I.; Okolie, J.A.; Paramasivam, P. Comprehensive Characterization of Some Selected Biomass for Bioenergy Production. *ACS Omega* **2023**, *8*, 43771–43791. [[CrossRef](#)] [[PubMed](#)]
43. Wang, J.; Zhang, S.; Guo, X.; Dong, A.; Chen, C.; Xiong, S.; Fang, Y.; Yin, W. Thermal Behaviors and Kinetics of Pingshuo Coal/Biomass Blends during Copyrolysis and Cocombustion. *Energy Fuels* **2012**, *26*, 7120–7126. [[CrossRef](#)]
44. Yao, X.; Xu, K.; Liang, Y. Comparing the Thermo-Physical Properties of Rice Husk and Rice Straw as Feedstock for Thermochemical Conversion and Characterization of their Waste Ashes from Combustion. *Bioresources* **2016**, *11*, 10549–10564. [[CrossRef](#)]
45. El-Sayed, S.E.; Abdelaziz, N.A.; El-Housseiny, G.S.; Aboshanab, K.M. Nanosponge hydrogel of octadecyl 3-(3,5-di-tert-butyl-4-hydroxyphenyl) propanoate of *Alcaligenes faecalis*. *Appl. Microbiol. Biotechnol.* **2024**, *108*, 100. [[CrossRef](#)] [[PubMed](#)]
46. Liang, R.; Chen, C.; Tao, J.; Xu, Y.; Song, M.; Cheng, Z.; Yan, B.; Chen, G. Thermal kinetic parameters based classification method of residual waste oriented for efficient energy utilization. *J. Clean. Prod.* **2024**, *439*, 140914. [[CrossRef](#)]
47. Ben Talouba, I.; Diop, A.; Neveu, K.; Balland, L.; Brodu, N.; Mouhab, N. Nitration of biodiesel by acetyl nitrate: Kinetic study and chemical safety parameters. *Thermochim. Acta* **2024**, *731*, 179647. [[CrossRef](#)]
48. Cai, J.; Huang, Q.; Chen, H.; Zhang, T.; Niu, B.; Zhang, Y.; Long, D. Evaluating two stages of silicone-containing arylene resin oxidation via experiment and molecular simulation. *Chin. J. Chem. Eng.* **2024**, *66*, 189–202. [[CrossRef](#)]
49. Li, M.; Zhang, D.; Han, Z.; Jiang, L. Thermal oxidation characteristics of polystyrene with different particle sizes based on the traditional kinetic approaches and distributed activation energy model. *J. Therm. Anal. Calorim.* **2024**, *149*, 993–1001. [[CrossRef](#)]
50. Wakimoto, S.; Matsukawa, Y.; Aoki, H. New criteria to select reasonable hyperparameters for kinetic parameter estimation in distributed activation energy model (DAEM) by using neural network. *Chem. Eng. Sci.* **2024**, *285*, 119597. [[CrossRef](#)]
51. Song, Y.; Jin, Z.; Zhang, J.; Jin, B.; Peng, R. Spiral gas-solid two-phase flow continuous mechanochemical synthesis of salophen complexes and catalytic thermal decomposition of ammonium perchlorate. *Dalton Trans.* **2024**, *53*, 3765–3776. [[CrossRef](#)] [[PubMed](#)]
52. Kumar, R.; Dubey, P.; Mondal, M.K. Analysis of kinetics, mechanism, thermodynamic properties and product distribution for pyrolysis of Ni-Fe impregnated coconut husk. *Renew. Energy* **2024**, *222*, 119972. [[CrossRef](#)]
53. Gao, N.; Zhang, J.; Quan, C.; Wang, J. Research on the characteristics of pressured pyrolysis products of marine plastics. *J. Anal. Appl. Pyrolysis* **2024**, *177*, 106327. [[CrossRef](#)]
54. Nan, W.; Ji, W.; Yuan, Y.; Yuan, Z.; Sun, Y. Pyrolysis Empirical Modeling of Polyester Glass Fiber Reinforced Plastics Using Sestak-Berggren Model Method. *J. Therm. Sci.* **2024**, *33*, 725–738. [[CrossRef](#)]
55. Zhang, C.; Wu, L.; Kang, R.; Bin, F.; Dou, B. Precise in-situ infrared spectra and kinetic analysis of gasification under the H₂O or CO₂ atmospheres. *Int. J. Hydrogen Energy* **2024**, *52*, 46–57. [[CrossRef](#)]
56. Li, B.; Zhang, W.; Jia, F.; Yang, T.; Bai, S.; Zhou, Q. Research on the Combustion Performance of Municipal Solid Waste in Different Sorting Scenarios: Thermokinetics Investigation via TG-DSC-FTIR-MS. *ACS Omega* **2023**, *9*, 1206–1215. [[CrossRef](#)]

57. Ren, J.; Jiang, J.; Wang, J.; Yuan, X.; Wang, A. Variable frequency microwave induced CO₂ Boudouard reaction over biochar. *Biochar* **2024**, *6*, 20. [[CrossRef](#)]
58. Zhu, Y.; Huo, G.; Yang, W.; Liu, H.; Zhang, W.; Cheng, W.; Yang, H.; Wang, Z.; Jin, Y.; Zhao, H. Catalytic pyrolysis of duckweed with phosphoric acid: Pyrolysis behavior and kinetics analysis. *J. Anal. Appl. Pyrolysis* **2024**, *177*, 106384. [[CrossRef](#)]
59. Huang, Q.; Gong, B.; Habibullah; Wang, Z.; Wang, Y.; Yan, Y.; Chen, Y.; Wu, C. Hydrogen generation behaviors from hydrolysis of cold-welding free magnesium-calcium hydride-expanded graphite composites. *J. Power Sources* **2024**, *595*, 234004. [[CrossRef](#)]
60. Aldossari, H.M.; Salam, A.A. COVID-19 infections, recoveries, and mortality: An ANOVA model of locations and administrative areas in Saudi Arabia. *Front. Public Health* **2024**, *12*, 1281289. [[CrossRef](#)]
61. JB/T 8583-2008; Resin coated sand for foundry. China Machine Press: Beijing, China, 2008.
62. JB/T 3823-2013; Hot box resin for foundry. China Machine Press: Beijing, China, 2014.
63. GB/T 30732-2014; Proximate analysis of coal—Instrumental method. Standards Press of China: Beijing, China, 2014.
64. GB/T 15445.2-2006; Representation of results of particle size analysis—Part 2: Calculation of average particle size/diameters and moments from particle size distributions. Standards Press of China: Beijing, China, 2006.
65. Tian, L.; Zhou, Y.; Xie, G.; Li, R.; Yu, X. Ecofriendly Cold Ramming Paste for an Aluminum Electrolysis Cell with Furan Resin As a Binder. *Ind. Eng. Chem. Res.* **2012**, *51*, 6018–6024. [[CrossRef](#)]
66. Li, Y.; Zhou, J.; Yin, Y.; Wan, P.; Ji, X.; Shen, X.; Qian, X.; Peng, X.; Qi, Y. Present status and prospect of resin-bonded sand technology for casting in China. *Foundry* **2022**, *71*, 251–270.
67. Murthy, I.N.; Rao, J.B. Investigations on Physical and Chemical Properties of High Silica Sand, Fe-Cr Slag and Blast Furnace Slag for Foundry Applications. *Procedia Environ. Sci.* **2016**, *35*, 583–596. [[CrossRef](#)]
68. Coronado, M.; Andres, A.; Cheeseman, C.R. Acid gas emissions from structural clay products containing secondary resources: Foundry sand dust and Waelz slag. *J. Clean. Prod.* **2016**, *115*, 191–202. [[CrossRef](#)]
69. Almusafir, R.; Smith, J.D. Thermal Decomposition and Kinetic Parameters of Three Biomass Feedstocks for the Performance of the Gasification Process Using a Thermogravimetric Analyzer. *Energies* **2024**, *17*, 396. [[CrossRef](#)]
70. Gupta, J.; Konyshva, E.Y.; Papadikis, K. Functions of local structural surrounding in activity of Ca-containing catalysts for vapor upgrading during biomass thermal decomposition. *Fuel Process. Technol.* **2023**, *252*, 107973. [[CrossRef](#)]
71. Li, Y.; Zhao, H.; Sui, X.; Wang, X.; Ji, H. Studies on individual pyrolysis and co-pyrolysis of peat-biomass blends: Thermal decomposition behavior, possible synergism, product characteristic evaluations and kinetics. *Fuel* **2022**, *323*, 124426. [[CrossRef](#)]
72. Jiang, B.; Yao, Q.; Su, M.; Li, J.; Lu, K.; Ding, D.; Hong, H. Study on the suppression characteristics and mechanism of ABC powder on pulverized coal explosion based on the analysis of thermal decomposition characteristics and reaction kinetics. *Process Saf. Environ. Prot.* **2024**, *181*, 143–155. [[CrossRef](#)]
73. Daniel, S.; Vnaraj, R.; Baskar, S.; Manivasagam, V.R.; Jerdy, A.C.; Armugam, S.; Kim, S.C. Citric Acid Recovery and Methanol Production from a Waste Food Fruit Sample by Thermal Decomposition of a Reusable Zinc Citrate Complex. *ACS Sustain. Chem. Eng.* **2022**, *10*, 15680–15691. [[CrossRef](#)]
74. Chen, K.S.; Yeh, R.Z. Pyrolysis kinetics of epoxy resin in a nitrogen atmosphere. *J. Hazard. Mater.* **1996**, *49*, 105–113. [[CrossRef](#)]
75. Mu, L.; Chen, J.; Yin, H.; Song, X.; Li, A.; Chi, X. Pyrolysis behaviors and kinetics of refining and chemicals wastewater, lignite and their blends through TGA. *Bioresour. Technol.* **2015**, *180*, 22–31. [[CrossRef](#)] [[PubMed](#)]
76. Wu, C.; You, J.; Wang, X. Thermal decomposition mechanism and kinetics of gemcitabine. *J. Anal. Appl. Pyrolysis* **2018**, *130*, 118–126. [[CrossRef](#)]
77. Yang, M.; Chen, X.; Wang, Y.; Yuan, B.; Niu, Y.; Zhang, Y.; Liao, R.; Zhang, Z. Comparative evaluation of thermal decomposition behavior and thermal stability of powdered ammonium nitrate under different atmosphere conditions. *J. Hazard. Mater.* **2017**, *337*, 10–19. [[CrossRef](#)] [[PubMed](#)]
78. Chen, J.; Xie, C.; Liu, J.; He, Y.; Xie, W.; Zhang, X.; Chang, K.; Kuo, J.; Sun, J.; Zheng, L.; et al. Co-combustion of sewage sludge and coffee grounds under increased O₂/CO₂ atmospheres: Thermodynamic characteristics, kinetics and artificial neural network modeling. *Bioresour. Technol.* **2018**, *250*, 230–238. [[CrossRef](#)]
79. Jiang, L.; Yuan, X.; Li, H.; Xiao, Z.; Liang, J.; Wang, H.; Wu, Z.; Chen, X.; Zeng, G. Pyrolysis and combustion kinetics of sludge-camphor pellet thermal decomposition using thermogravimetric analysis. *Energy Convers. Manag.* **2015**, *106*, 282–289. [[CrossRef](#)]

Disclaimer/Publisher’s Note: The statements, opinions and data contained in all publications are solely those of the individual author(s) and contributor(s) and not of MDPI and/or the editor(s). MDPI and/or the editor(s) disclaim responsibility for any injury to people or property resulting from any ideas, methods, instructions or products referred to in the content.